

The Role of Grain Boundaries in Nanoscale Sintering: An Atomistic Simulation Study

Jesse M. Sestito^{a,b}, Fadi Abdeljawad^{b,c,*}, Tequila A. L. Harris^a, Yan Wang^a,
Allen Roach^b

^a*George W. Woodruff School of Mechanical Engineering,
Georgia Institute of Technology, Atlanta, Georgia, 30332, USA*

^b*Sandia National Laboratories, Albuquerque, New Mexico, 87185, USA*

^c*Department of Mechanical Engineering, Clemson University, Clemson, South Carolina,
29634-0921, USA*

Abstract

Sintering is a processing technique used to produce bulk materials from powder compacts. Recently, sintering has been the subject of active research for its relevance to a wide range of applications, such as additive manufacturing and processing of bulk nano-crystalline materials. Of particular interest is the role of grain boundaries (GBs) on sintering mechanisms, cooperative mass transport, and pore shrinkage rates. Herein, atomistic simulations are leveraged to investigate sintering kinetics, particle neck growth, and densification rates of nanoscale particles as a function of GB character. The two-particle geometry is used to examine particle neck growth rates and crystallographic re-orientation events, and report relative GB diffusion rates as a function of GB misorientation. For the three-particle configuration, simulation results reveal a plethora of pore shrinkage profiles ranging from complete shrinkage to stagnant response depending on the GBs present in the system. This is the first atomistic study that systematically examines the role of GB character on pore shrinkage rates. Our results highlight the need to revisit continuum sintering treatments in order to account for the anisotropy in GB properties.

Keywords: Nanoscale Sintering, Atomistic Simulations, Grain Boundary, Additive Manufacturing

*Corresponding author. e-mail: fabelj@clemson.edu; Tel.: (864) 656-5639; fax: (864) 656-4435.

1. Introduction

Sintering is a thermal processing technique commonly used to consolidate a powder compact and converts it into one with strength and structural integrity [1, 2]. The main driving force for sintering is the reduction in the interfacial contribution to the total free energy of the sintered body [3, 4]. Upon heating, particles sinter bond together leading to particle neck growth and densification, i.e., elimination of internal porosity [4]. In addition to dimensional changes due to pore shrinkage, many properties of the sintered powder, such as strength, ductility, conductivity, and piezoelectric, undergo significant changes as a result of particle bonding during sintering [2, 5–7].

Recently, sintering has been the subject of active research for its relevance to a wide range of processes, such as direct ink write [8–10] and powder bed [11] additive manufacturing. Furthermore, sintering of nanoscale powders presents many potential advantages, such as lower processing temperatures and shorter times [12–16] and the possibility of fabricating dense objects with small grain sizes, and thus enhanced properties [12, 17–20].

In crystalline materials, when differently orientated particles bond at the neck region, internal interfaces (i.e., grain boundaries) form, which along with free surfaces contribute to both the energy landscape of the powder undergoing sintering and the kinetics of the process. The role of free surfaces and grain boundaries (GBs) becomes dominant when the average particle size in a powder compact is reduced into the nanoscale due to the increased surface-to-volume ratio and number of contact points between particles [2, 21, 22]. One of the key challenges with nanoscale sintering is the ability to mitigate grain coarsening processes while enhancing pore densification mechanisms in order to achieve dense nanocrystalline materials [19, 23, 24].

Classically, analytical sintering treatments of crystalline materials yield dynamical scaling relations for the temporal evolution of a microstructural feature of interest, typically particle neck width or pore densification, as a function of the dominant mass transport mechanism, e.g., surface, GB, bulk, and evaporation/condensation [1, 25–29]. Most of these treatments rely on the isotropy assumption for the interfacial properties and studies of the role of GB anisotropy on sintering mechanisms and densification rates remain elusive [3]. In general, five macroscopic degrees of freedom (DOF) define the GB geometry: three for misorientation and two for the plane normal [30]. It is well established by now that GB properties (e.g., energy, mobility, diffusion) are highly dependent on the GB geometric DOF [31, 32]. Therefore, the

sintering behavior (i.e., GB migration rates, microstructural evolution, and pore densification rates) of a particle compact is highly dependent on the GBs present in the powder and associated anisotropies in their properties.

Experimental studies of nanoscale sintering examine the role of particle purity and process control [33, 34], surface structure [35, 36], mass transport mechanisms [23], and crystallographic orientation of particles [37] on particle neck growth and densification processes. As an example, Fig. 1 (taken from Ref. [35]) depicts a high resolution electron microscopy image of an ensemble of nanoscale particles undergoing sintering, where several interface processes are observed, such as atomically rough neck regions, faceted profiles, and discrete contact angles.

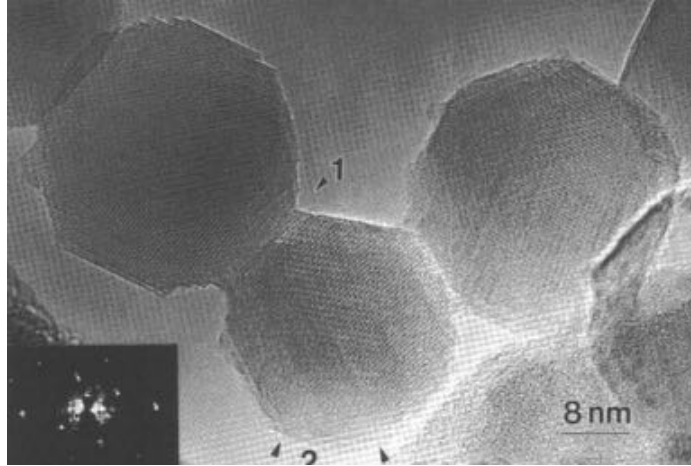


Figure 1: High resolution electron microscopy image of an ensemble of nanoscale alumina particles undergoing sintering. Atomically rough neck regions, faceted profiles, and discrete contact angles can be observed. Taken from Ref. [35].

Atomistic simulations provide a suitable approach to investigate at a fundamental level the role of GBs on the sintering behavior of nanoparticles. Recently, Molecular Dynamics (MD) have been used to study nanoscale sintering in a wide range of materials, such as Al [38, 39], Au [40], Si [41, 42], Ni [43, 44], Ag [45], Cu [46], Fe [47, 48], and W [29]. Ding [49] investigated sintering of nanoparticles using a pairwise Lennard-Jones interatomic potential. Song and Wen [50] examined the role of particle size on the sintering behavior of two nickel nano-particles with the same crystallographic orientation, i.e., no GB between them. Rcidiacono et al. [51] studied the effects

of particle size and temperature on the sintering behavior of two gold nanoparticles, where particles in the range of 9.5 Å and 25 Å were examined. In a recent study by Lange et al. [52], the authors examined deformation mechanisms in a system of two 5 nm Au nanoparticles that were sintered to 5 ns.

While the aforementioned atomistic studies shed light on several mechanisms involved in nanoscale sintering, the role of GBs in the sintering behavior and pore shrinkage kinetics has not been studied systematically. In this work, MD simulations are leveraged to examine sintering kinetics of nanoscale nickel particles. More specifically, we seek to quantify the role of GBs on particle neck formation and growth, pore shrinkage, and densification rates. In this work, two geometries are explored. First, the two-particle configuration, where two particles with different crystallographic orientations are brought into contact with each other, is used to examine particle neck growth and relative GB diffusion rates as a function of GB misorientation. The second is the three-particle geometry, where three equi-sized particles are spatially placed such that their centers form the vertices of an equilateral triangle, leading to the formation of an internal pore, i.e., a tricusp. Simulation results reveal a plethora of pore shrinkage profiles ranging from complete shrinkage to stagnant response depending on the GBs present in the system. The rest of the paper is organized as follows. The computational set-up and simulation procedure are presented in Section 2. Simulation results of two-particle geometry are presented and discussed in Section 3.1, while Section 3.2 presents the results for the three-particle geometry. Finally, Section 4 provides concluding remarks and summary of the work.

2. Simulation Method and Computational Set-up

In this work, two different geometries are used in order to explore the sintering behavior of nanoscale particles. The first is the two-particle configuration, where two equi-sized particles with crystallographic orientations that are varied independently are brought in contact with each other and evolved over time at the desired sintering temperature. The sintering behavior of this geometry is quantified by monitoring the formation and growth of the particle neck region, and temporal evolution of the particles' centers of mass and total surface area as a function of the crystallographic orientations of the two particles. The second configuration we explore is the three-particle geometry, where three equi-sized particles are spatially positioned such that

their centers form the vertices of an equilateral triangle, leading to the formation of a closed internal pore, or a tricusp. The crystallographic orientations of the particles are varied independently leading to the formation of three GBs at the neck regions between the particles. Sintering kinetics for this geometry are quantified by monitoring the shrinkage of the internal pore as a function of the GBs present in the system.

In our MD simulations, nanoscale cylindrical disks that are periodic along the out-of-plane cylindrical axis are used in lieu of three-dimensional (3D) particles. This is done in order to circumvent the computational expenses associated with simulating 3D particles, each of which could contain hundreds of thousands of atoms. This approach allows us to simulate nanoscale particles with reasonable computational costs and probe sintering kinetics as a function of many GB types. For the remainder of this work, we will refer to these cylindrical disks as particles. For both the two- and three-particle configurations, the cylindrical axis is aligned with the reference z-axis, and the angle/axis pair, i.e., $\theta/\langle UVW \rangle$, is used for the GB misorientation DOF [30, 53].

The MD simulations are performed using the Ni embedded atom method (EAM) interatomic potential developed by Foiles and Hoyt [54], which had been used to calculate the energy and mobility of several GBs in Ni [31, 32]. For this potential, the equilibrium lattice constant at 0 K is $a = 3.52$ Å and the melting temperature $T_m = 1565$ K [54]. Atomistic simulations are performed using Large-scale Atomic/Molecular Massively Parallel Simulator (LAMMPS) [55, 56] and visualizations are done with the Open Visualization Tool (Ovito) [57]. The numerical time step used to advance atoms' positions and velocities is set to 1 fs.

For the two-particle configuration, the initial atomistic structures are generated as follows: i) A 0 K equilibrated periodic atomistic box is generated with the crystal [001], [010], and [001] directions aligned with the reference x, y, and z directions, respectively. ii) Atoms are assigned to each particle based on user defined geometric parameters (i.e., particle diameter D_p and center $\mathbf{c}_p = (c_x, c_y)$). The remaining atoms outside the cylindrical particles are deleted. iii) The two particles are then rotated by an equal but opposite angle $\theta/2$ about their common $[UVW] = [001]$ cylindrical axis. Care is taken to ensure that the simulation box is large enough so that atoms from the two particles do not interact across the simulation box's boundaries. This construction results in a two-particle geometry with an initial misorientation across the particle neck region that is described by $\theta/[001]$. Figure 2(a) shows

the two-particle configuration employed in this study. Here, we consider particle diameters ranging from 5 to 40 nm and misorientation angles θ ranging from 5° to 45° . The thickness of the particles along the periodic out-of-plane direction is set to ≈ 1.41 nm.

Generation of the initial atomistic structures for the three-particle geometry follows in a similar fashion: i) For each sintering simulation, a specific GB misorientation is targeted, where a 0 K equilibrated atomistic box is first created, with the crystal $[UVW]$ direction aligned with the reference z-axis. ii) Three equi-sized cylindrical disks (particles) of diameter D_p are spatially positioned such that their centers form the vertices of an equilateral triangle. Atoms that are spatially located within each particle are selected and assigned a unique atom type (for identification purposes). The remaining atoms outside the three particles are deleted. Figure 2(b) shows the three-particle geometry, where the three particles share their out-of-plane $[UVW]$ crystal direction. iii) The particle labeled 1 in Figure 2(b) is left unrotated (i.e., has the same crystal direction of the original atomistic box), whereas particles labeled 2 and 3 (i.e., lower left and right, respectively) are rotated about their common $[UVW]$ crystal direction by an equal but opposite angle $\theta/2$. This configuration results in two asymmetric tilt GBs with a misorientation angle of $\theta/2$ (between particles 1-2 and 1-3) and one symmetric tilt GB with a misorientation angle of θ (between particles 2-3). Three different cases for $[UVW]$ are explored, i.e., $[UVW] = [001]$, $[110]$, and $[111]$, with several rotation angles $\theta/2$ for each case. The crystallographic orientation for the unrotated particle 1 is chosen as follows: For $[UVW] = [001]$, the crystal $[100]$ and $[010]$ (dark and white axes in Figure 2(b)) are aligned with the reference x- and y-directions, respectively. For $[110]$, they are $[1\bar{1}4]$ and $[2\bar{2}\bar{1}]$. Finally, for rotations about $[111]$, they are $[2\bar{1}\bar{1}]$ and $[01\bar{1}]$.

Following the initial system construction given by the aforementioned steps, atoms whose separation distance is less than 0.3 \AA are deleted and a conjugate gradient energy minimization at 0 K is performed while allowing the simulation box to expand or contract in order to achieve zero pressure on the simulation box. Then, the initial structures are isothermally annealed at 300 K for 0.5 ns using the Nosé-Hoover thermostat [58–60]. This creates a trajectory in the phase space that is consistent with the canonical (NVT) ensemble. After this initial low temperature annealing step, the sintering protocol starts, where the atomic structures are heated quickly from 300 K to 1000 K ($\approx 0.64 T_m$ for the Ni inter-atomic potential used in this study) over a period of 0.5 ns, then held at 1000 K for a period of 40 ns.

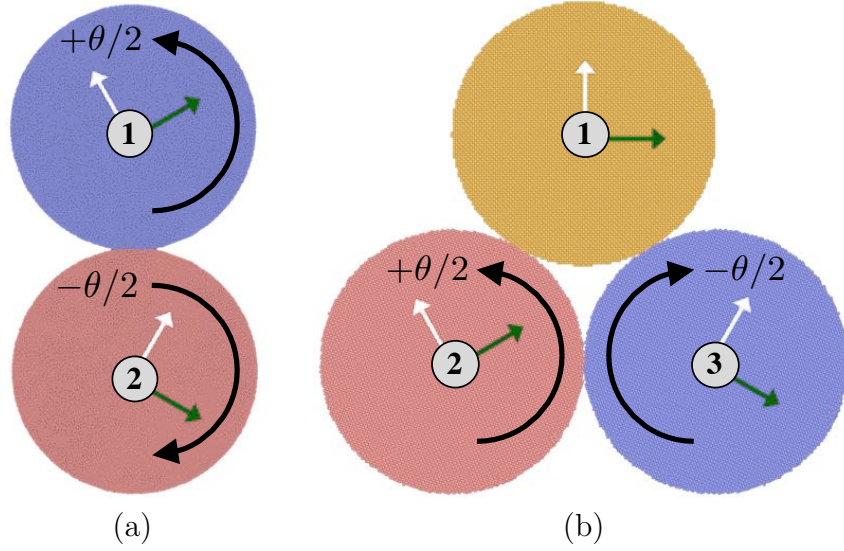


Figure 2: Atomistic simulation setup for: (a) the two-particle geometry, where two particles are rotated by an equal but opposite angle, $\theta/2$, about their common out-of-plane $[001]$ crystal axis, and (b) the three-particle geometry, where three particles, sharing their crystal out-of-plane axis $[UVW]$, are placed such that their centers form the vertices of an equilateral triangle. The bottom two particles, labeled 2 and 3, are rotated by an equal but opposite angle, $\theta/2$, about their common out-of-plane $[UVW]$ axis, while the particle labeled 1 is left unrotated.

Several values for the thickness of the cylindrical particles in the out-of-plane direction are examined in order to ensure that the results reported in this work are not dependent on the thickness. As an example, Fig. 3 depicts the evolution of the shrinkage of the internal pore for the three-particle system with $[UVW] = [001]$ and $\theta/2 = 40^\circ$ as a function of the system's out-of-plane thickness. Here, the commonly used pore shrinkage metric $S(t)$ (i.e., percent change of the in-plane pore area) is used, which is given by [1]

$$S(t) = \frac{A(0) - A(t)}{A(0)} = 1 - \left(\frac{R(t)}{R(0)} \right)^2, \quad (1)$$

where $A(t) \propto R^2(t)$ is the in-plane area of the internal pore at time t and $R(t)$ is the effective in-plane pore radius. Given the periodic nature along the out-of-plane direction for this geometry, pore shrinkage is driven by the

reduction in the in-plane area. It can be seen that our choice for the system thickness yields convergent results in terms of pore shrinkage kinetics.

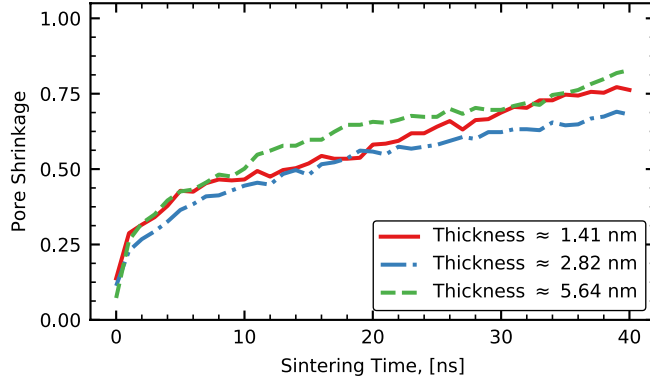


Figure 3: For the three-particle system with $[UVW] = [001]$ and $\theta/2 = 40^\circ$, temporal evolution of the internal pore shrinkage [refer to Eq. 1] for various values of the system’s out-of-plane thickness.

3. Results

3.1. Two-particle geometry

In this section, simulation results of the sintering behavior, particle neck formation and growth, and interface evolution of the two-particle geometry are discussed. As described in Section 2, two particles are rotated about their common $[001]$ crystal axis by an equal but opposite angle $\theta/2$, i.e., a misorientation described by $\theta/[001]$, and then brought into contact with each other. Several initial misorientation angles θ (ranging from 5° to 45°) and particle diameters D_p (ranging from 5 nm to 40 nm) are explored in order to examine the role of GB type and particle size on the sintering behavior of the two-particle geometry.

First, we examine particle neck formation and growth. Figure 4 shows snapshots of the two-particle configuration for the case with $D_p = 20$ nm and $\theta = 45^\circ$ at simulation times of (a) $t = 0$ (the initial stage before the temperature ramp up to 1000K), (b) $t = 20$ ns, and (c) $t = 40$ ns. In all panels, the common neighbor analysis (CNA) metric is used to color atoms, where FCC atoms within each particle are assigned a unique color (red and

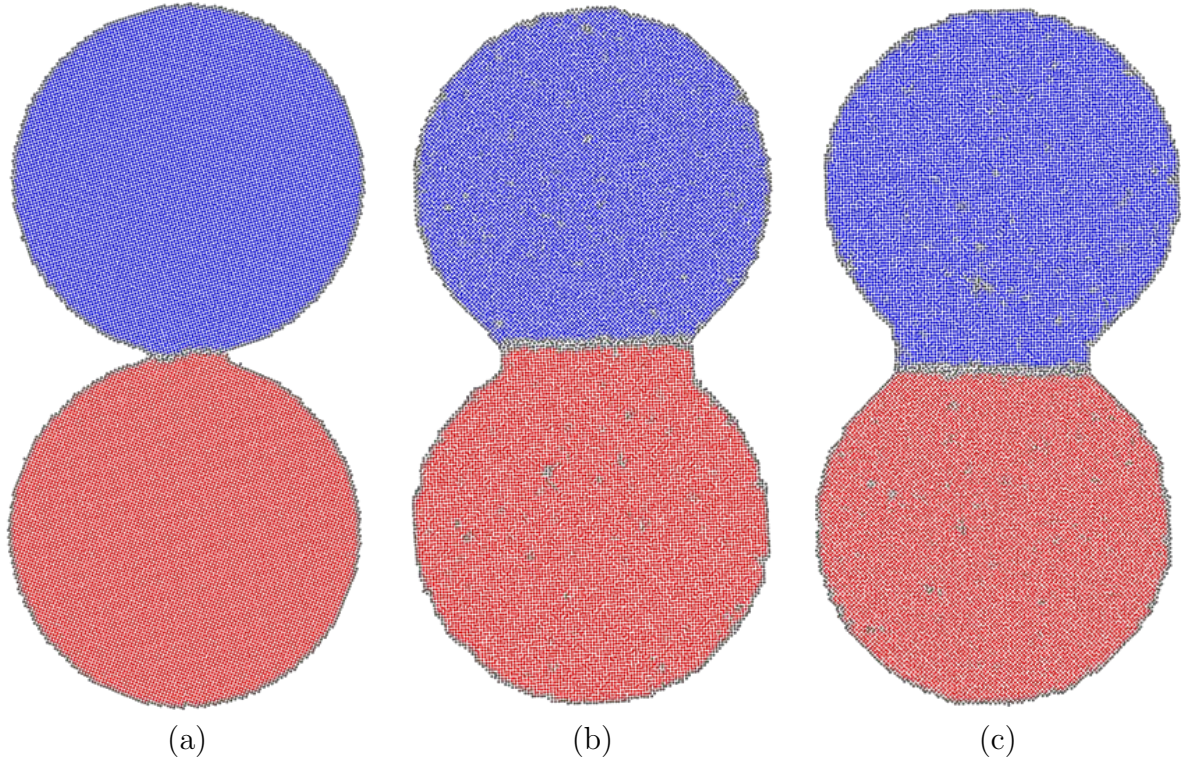


Figure 4: For the two-particle geometry with $D_p = 20$ nm and $\theta = 45^\circ$, snapshots depicting the microstructural evolution at (a) the initial stage before the temperature ramp up to 1000 K, and after (b) 20 ns and (c) 40 ns of sintering at 1000 K. With the aid of the CNA metric, atoms within each particle are assigned a unique color, and ones at GBs and free surfaces are colored dark gray.

blue) and ones without local FCC ordering (at free surfaces or GBs) are colored dark gray. As the structure evolves over time, the neck region between the two particles begins to form and grow. Moreover, free surfaces around the neck region evolve and reconstruct (i.e., develop faceted profiles) in order to achieve an equilibrium dihedral angle as a result of the balance of free surface and GB energies [4]. This effect has been experimentally observed in nanoparticles and Fig. 1 (taken from Ref. [35]) shows an example of this effect in alumina nanoparticles.

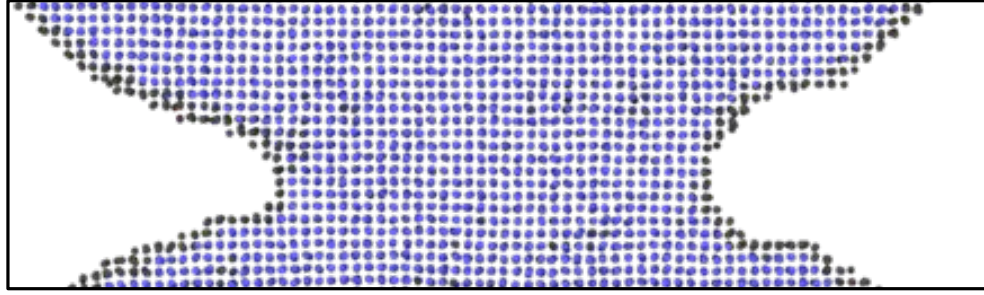
Next, the microstructural evolution of the two-particle system with various particle sizes and misorientation angles is analyzed. Two-particle systems that undergo rigid body rotation and crystallographic re-orientations across

Table 1: For a given two-particle system with a particle diameter D_p and misorientation angle θ , analysis depicting systems that form GBs (gray cells) and ones that do not form GBs, i.e., undergo rigid body rotation (white cells).

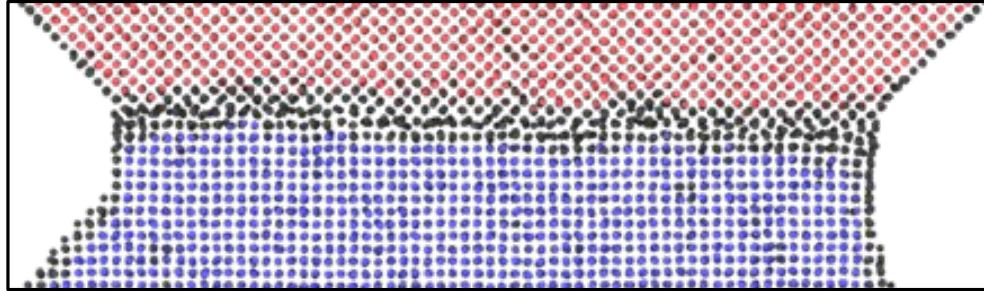
| D_p [nm] | Angle θ [Deg.] | | | | | | | | |
|---------------|-----------------------|----|----|----|----|----|----|----|----|
| | 5 | 10 | 15 | 20 | 25 | 30 | 35 | 40 | 45 |
| 5 | | | | | | | | | |
| 10 | | | | | | | | | |
| 20 | | | | | | | | | |
| 30 | | | | | | | | | |
| 40 | | | | | | | | | |

the neck region are identified and the results are shown in Table 1, where cells colored gray (white) correspond to systems that form (do not form) GBs. It can be seen that for $\theta \lesssim 25^\circ$ about the $[001]$ axis, particles regardless of their size undergo rigid body rotation and achieve a uniform crystallographic orientation across the neck region. For example, Fig. 5 shows close-up views of the neck region for the system with $D_p = 20$ nm and θ value of (a) 20° and (b) 45° at a simulation time of $t = 40$ ns. For $\theta = 20^\circ$, the two particles rotate with respect to each other leading to re-alignment of their crystallographic orientations and no GB forms between them. This in turn results in stagnant neck growth kinetics as will be discussed later in this section. On the other hand, when $\theta = 45^\circ$ a GB forms between the two particles and the neck region continues to grow over time. Free surfaces near particle neck regions evolve into faceted profiles [refer to Figure 5(b)] as a result of surface energy anisotropy (the plane normal DOF) and the balance of GB and free surface energies, i.e., Young’s equation [4]. For systems with $\theta \lesssim 25^\circ$, the crystallographic re-orientation of the two particles occurs at relatively fast rates (during the temperature ramp up in some instances). Rigid body rotations have been observed in several studies of nanoparticle coalescence [37, 49].

For the remainder of this section, we focus our attention on the sintering behavior and densification rates for the two-particle geometry with a particle diameter $D_p = 40$ nm. First, the separation distance D_{CM} between the two particles’ centers of mass is calculated for several misorientation angles θ . At any given instance in time, a boolean operation using the CNA metric is performed, where all FCC atoms belonging to each particle are identified



(a)



(b)

Figure 5: At a simulation time of $t = 40$ ns, close-up views of the neck region for the two particle geometry with $D_p = 20$ nm and θ of (a) 20° and (b) 45° . Atoms are colored according to the CNA metric, where FCC atoms within each particle are assigned a unique color and ones without local FCC ordering (free surfaces and GBs) are colored dark gray.

and used to calculate the two particles' centers of mass, denoted by \mathbf{r}_1 and \mathbf{r}_2 . The temporal evolution of $D_{CM} = |\mathbf{r}_1 - \mathbf{r}_2|$ provides a measure of how particles' centers of mass approach each other as the neck region between them grows over time, and is used as a densification metric. Figure 6 shows plots of the temporal evolution of D_{CM} for the two-particle geometry with a particle diameter of 40 nm. As the systems evolve over time, D_{CM} decreases indicating particle neck growth. Further, it can be clearly seen that the evolution of D_{CM} is highly sensitive to the GBs present in the system. At the end of the simulations, D_{CM} decreased the most in systems with $\theta = 35^\circ$ and 40° , while ones with $\theta = 5^\circ, 10^\circ$, and 30° showed no, or very little, reduction in D_{CM} .

Next, the total free surface area and particle neck length are quantified as a function of time. Free surface area is calculated as follows: Delaunay

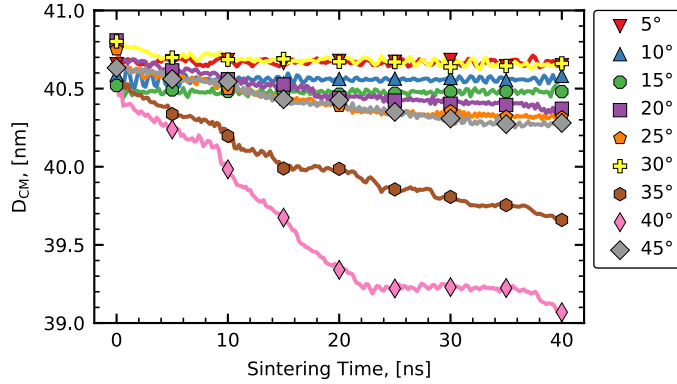


Figure 6: For the two-particle system with $D_p = 40$ nm, temporal evolution of the separation distance between the particles' centers of mass D_{CM} as a function of the misorientation angle θ .

tetrahedrization is obtained using the atoms in the system as a point set. A surface polyhedral mesh and its total area are obtained from the tetrahedron formed in the solid domain (i.e. the triangular faces of the tessellation that separates the solid domain from open space) [57, 61]. Figure 7 shows the temporal evolution of the total free surface area [Fig. 7(a)] and particle neck radius X [Fig. 7(b)] as function of time for several values of θ . Sintering leads to a reduction in free surface area and an associated increase in particle neck size. The trends observed in Figs. 6 and 7 show that the quantitative metrics describing the sintering behavior of the two particle-system exhibit large variations as a function of the GB present in these systems; an effect that highlights the paramount role that GBs play in sintering kinetics.

The sintering behavior of the two-particle system can be further quantified using dynamical scaling relations that describe the evolution of a microstructural feature of interest. As is typically done in classical treatments of the two-particle geometry, the particle neck radius X evolves according to [1, 25–29]

$$\frac{X^m}{R_p^{m-n}} = Ht, \quad (2)$$

where m and n are numerical constants that depend on the active mass transport mechanism, t is time, $R_p = D_{CM}/2$, and H is a parameter that

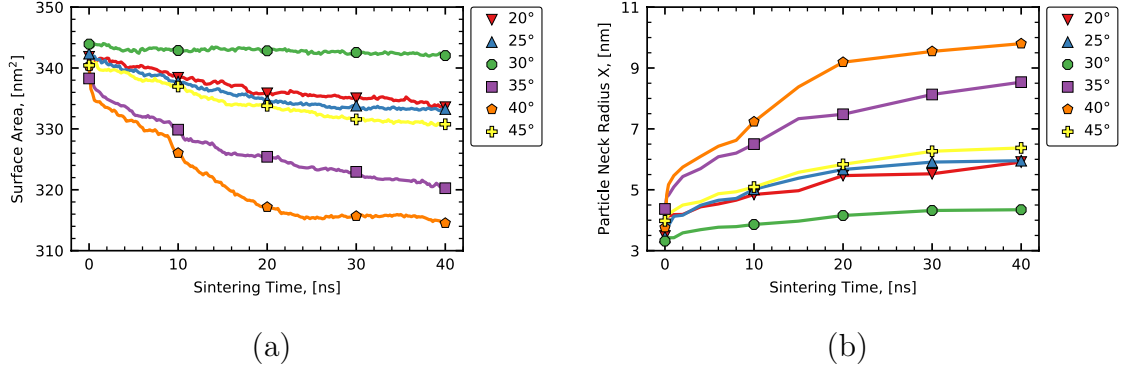


Figure 7: For the two-particle system with $D_p = 40$ nm, temporal evolution of the (a) total free surface area and (b) particle neck radius X as a function of the misorientation angle θ .

encompasses several material properties. When GB diffusion is the dominant mass transport mechanism, $(m, n) = (6, 4)$ and $H = H_{gb}$ is given by [1]

$$H_{gb} = \frac{96\bar{D}_{gb}\delta_{gb}\gamma_s\Omega}{k_B T}, \quad (3)$$

where \bar{D}_{gb} and δ_{gb} are the GB self diffusion coefficient and thickness, respectively. γ_s , Ω , k_B and T are the free surface energy, atomic volume, Boltzmann's constant, and absolute temperature, respectively. When mass transport along free surfaces dominates, $(m, n) = (7, 4)$ and $H = H_s$ and is given by [1]

$$H_s = \frac{56\bar{D}_s\delta_s\gamma_s\Omega}{k_B T}, \quad (4)$$

where \bar{D}_s and δ_s are the surface self diffusion coefficient and thickness, respectively.

Using the results for the temporal evolution of D_{CM} in Fig. 6 (with $R_p = D_{CM}/2$), particle neck radius in Fig. 7(b), and the scaling law given by Eq. (2), the value of the material parameter H as a function of θ can be obtained and the results are shown in Fig. 8(a). It can be seen that H_{gb} and H_s attain small values for $\theta < 30^\circ$, increase drastically for $\theta = 35^\circ$ and 40° , then decrease in values for $\theta = 45^\circ$. A close examination of Eqs. (3) and (4) reveals that the forms of H_{gb} and H_s only differ in the interfacial properties

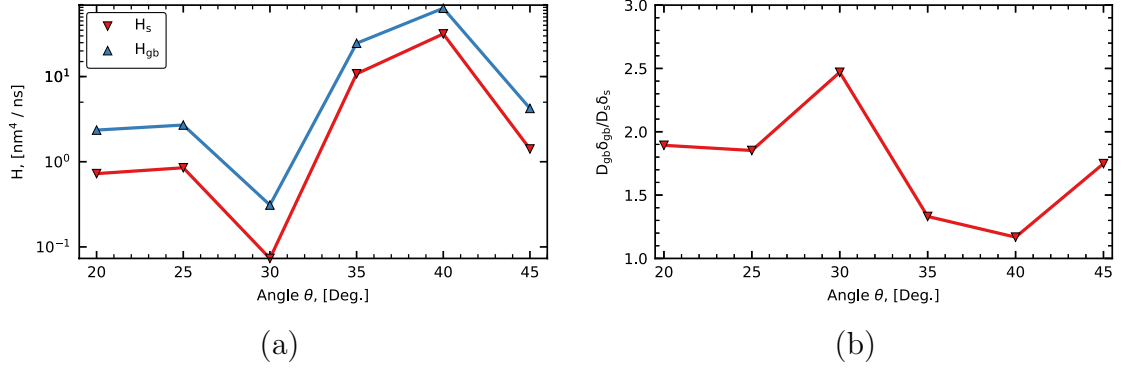


Figure 8: For the two-particle system with $D_p = 40$ nm, a plot of the (a) parameter H [refer to Eq. 2] under the assumption of GB diffusion (i.e., $H = H_{gb}$) and surface diffusion (i.e., $H = H_s$), and (b) ratio $\bar{D}_{gb}\delta_{gb}/\bar{D}_s\delta_s$ as a function of the misorientation angle θ .

(diffusivities and widths) that are relevant to the transport mechanism being considered. Motivated by the treatment of Johnson [62], the expressions for H_{gb} and H_s yield the ratio of GB to free surface diffusion as

$$\frac{\bar{D}_{gb}\delta_{gb}}{\bar{D}_s\delta_s} = \frac{56}{96} \frac{H_{gb}}{H_s}. \quad (5)$$

Therefore, using the data for H_{gb} and H_s [refer to Fig. 8(a)], the ratio $\bar{D}_{gb}\delta_{gb}/\bar{D}_s\delta_s$ is obtained as a function of θ and the results are shown in Fig. 8(b). Systems with $\theta = 35^\circ$ and 40° exhibit lower GB to surface diffusion ratios. Within the coincident site lattice (CSL) description of GB geometry, several high symmetry GBs result from misorientations in the range of $35^\circ < \theta < 45^\circ$ about $[001]$ (e.g., $\Sigma 5$ and $\Sigma 29b$ are characterized by a misorientation angle of 36.9° and 43.6° , respectively). The results depicted in Fig. 8(b) suggest that GB and surface diffusion are within the same order of magnitude at least for the range of angles explored in this study, and that high symmetry GBs are characterized by lower GB self diffusion. Our results of relative GB diffusion rates are in qualitative agreement with the experimental study by Johnson [63] and data collected therein [64–66].

Simulations results of the two-particle geometry underscore the critical role that GBs play in sintering kinetics. It is shown that some systems exhibit rapid particle neck growth, while others attain stagnant states with no or very little neck growth.

3.2. Three-particle geometry

While the two-particle geometry sheds light on the role of GBs on particle neck growth, it does not provide information about pore shrinkage kinetics, as this geometry by construction does not contain any internal pores. Therefore, in this section we examine sintering kinetics using the three-particle geometry, where three equi-sized particles are spatially placed such that their centers form the vertices of an equilateral triangle and leads to the formation of an internal pore. The crystallographic orientations of the three particles are chosen such that they all share the same out-of-plane $[UVW]$ crystal axis. Here, the sintering behavior of the three-particle geometry is quantified as a function of the GBs present in the system by monitoring shrinkage kinetics of the internal pore.

We first start by examining the microstructural evolution. Figure 9 shows snapshots of the atomic structures after annealing at 1000 K for 40 ns, where Figs. 9(a)-(c) depict the results for rotations about $[UVW] = [001]$ by an angle $\theta/2$ of (a) 0° , (b) 20° , and (c) 30° . Rotations about $[110]$ are shown in Figs. 9(d)-(f), for $\theta/2$ values of (d) 0° , (e) 40° , and (f) 80° . The results for $[111]$ rotations are shown in Figs. 9(g)-(i) for $\theta/2$ values of (g) 0° , (h) 40° , and (i) 60° . In all panels of Fig. 9, atoms are colored according to CNA, where green, red, and gray denote FCC, HCP, and none (defect). Further, Video 10 shows pore shrinkage dynamics for the system with $[UVW] = [111]$ and $\theta/2 = 40^\circ$.

It can be seen from Fig. 9 that a wide range of internal pore morphologies and shrinkage profiles result by varying the rotation axis, angle, or both. For example, complete shrinkage of the internal pore is reached for the case of $(\theta/2)/[UVW] = 40^\circ/[111]$ in Fig. 9(h) and Video 10, whereas very little shrinkage is observed for $0^\circ/[001]$ in Fig. 9(a) and $0^\circ/[110]$ in Fig. 9(d). Indeed, for the cases of 0° rotations about $[001]$, $[110]$, and $[111]$ (i.e., Figs. 9(a), (d), and (g), respectively) the adjoining particles have the same crystallographic orientations, and thus no GBs form during the annealing simulations. In such cases, free surface coarsening leads to partial neck formation. Due to the cubic crystal symmetry, some rotations about $[UVW]$ result in re-alignment of the crystal axes of the adjoining particles. For example, a rotation of $\theta/2 = 60^\circ$ about the $[111]$ axis, as in the case depicted in Figure 9(i), results in a total rotation of 120° between particles 2 and 3 ($[111]$ is a triad axis [67]). This in turn leads to a re-alignment of the crystal axes of particles 2 and 3, and thus no GB forms between them. Qualitatively, it

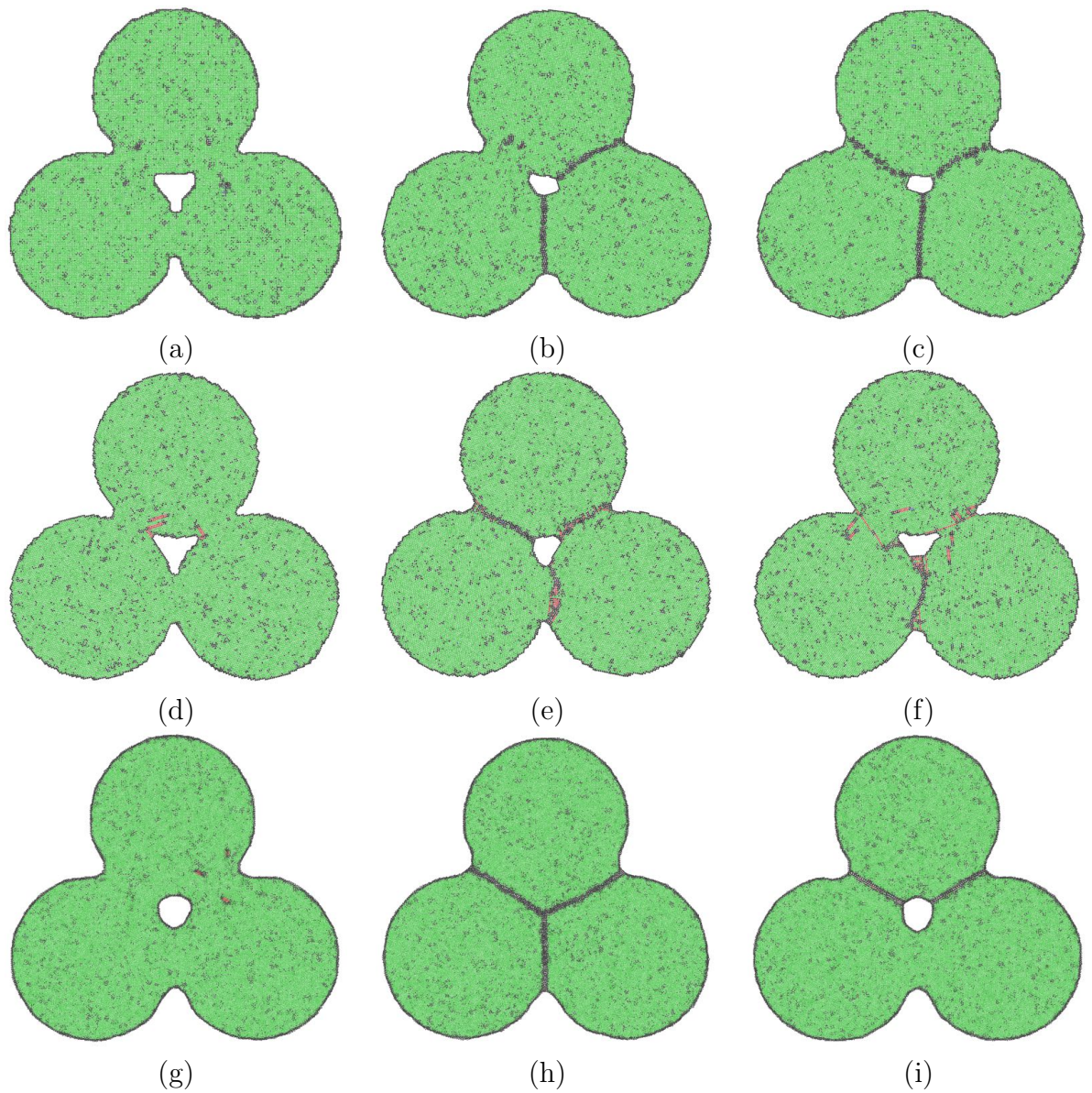


Figure 9: Snapshots of the three-particle geometry at a simulation time of 40 ns for rotations about the $[UVW]$ axis of (a)-(c) $[001]$, (d)-(f) $[110]$, and (g)-(i) $[111]$. The rotation angle $\theta/2$ is set to: (a) 0° , (b) 20° , (c) 30° , (d) 0° , (e) 40° , (f) 80° , (g) 0° , (h) 40° , (i) 60° .

Please include Video 1 in the online version

Figure 10: An animation depicting the microstructural evolution and internal pore shrinkage in the three-particle system with $[UVW] = [111]$ and $\theta/2 = 40^\circ$.

can be observed that internal pores shrink faster in systems, where all three GBs form between the particles [refer to Figs. 9(c), (e), and (h)].

Another interesting effect emerges for some angle/axis pairs, which is related to GB-pore interactions and the resulting GB break-away events. As an example, Fig. 11 depicts the temporal evolution of the three-particle geometry for the case of $(\theta/2)/[UVW] = 45^\circ/[001]$ at simulation times of (a) initial $t = 0$ after the temperature ramp-up to 1000 K, (b) $t = 34$ ns, (c) $t = 37.4$ ns, and (d) $t = 40$ ns. Owing to the cubic crystal symmetry, where $[001]$ is a tetrad axis [67], particles 2 and 3 have an equivalent crystallographic orientation, and no GB forms between them. In the initial stages, two GBs of the same misorientation between particles 1-2 and 1-3 form and grow as shown in Fig. 11(b). At later stages these GBs merge at the internal pore and break away from it as shown in Fig. 11(c). This in turn results in a two-grain structure with a single curved GB that undergoes curvature-driven flow. In addition, the isolated internal pore that is left in the structure is persistent, as it now requires bulk diffusion to shrink and collapse, which is a much slower process than diffusion along surfaces and GBs [68, 69].

The observations of pore shrinkage in Figs. 9 and 11 are made quantitative by monitoring the temporal evolution of the pore size $R(t)$ and the results are shown in Fig. 12 for $[UVW]$ of (a) $[001]$, (b) $[110]$, and (c) $[111]$. It can be seen that variations in pore shrinkage kinetics as a function of $\theta/2$ and $[UVW]$ are significant. For $[001]$ rotations, the trends in Fig. 12(a) suggest that the internal pore shrinks faster with increasing $\theta/2$. It can also be seen that some values of $\theta/2$ result in rapid densification (e.g., $\theta/2 = 40^\circ$ and 45°), whereas others yield stagnant states, i.e., the internal pore exhibits no or very little shrinkage. Rotations about the $[110]$ axis [refer to Fig. 12(b)] exhibit a similar trend, where enhanced pore shrinkage is observed with increasing $\theta/2$. For all angles examined in the $[110]$ case, the structures exhibit sluggish pore shrinkage kinetics, at least for the simulation times attained in this study. For rotations about $[111]$, Fig. 12(c) shows that some rotations are characterized by rapid pore shrinkage (e.g. $\theta/2 = 30^\circ$ and 40°), whereas others exhibit no or very little shrinkage. As discussed above, the three-particle configuration

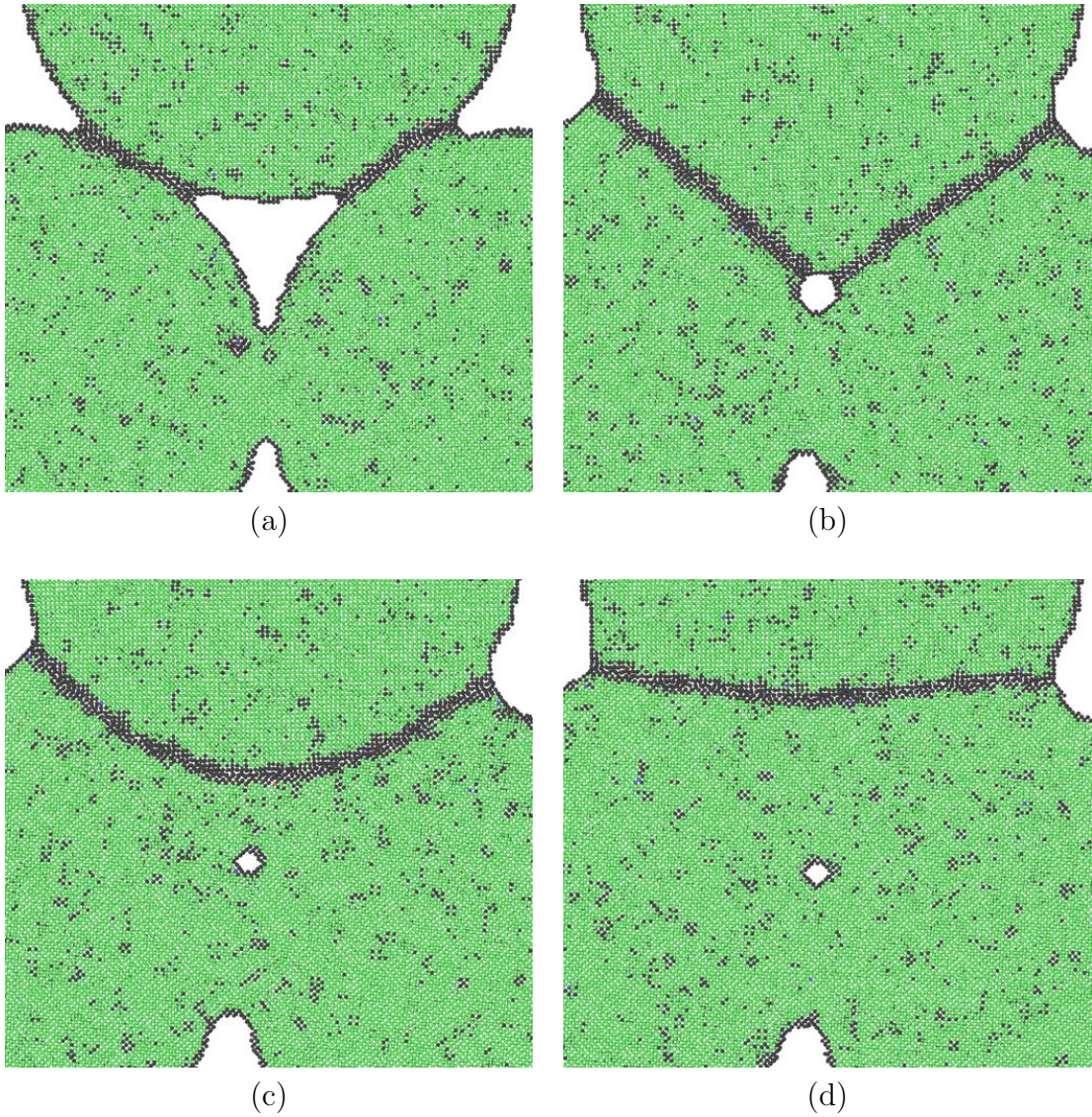


Figure 11: At $T = 1000$ K, the three-particle geometry with $(\theta/2)/[UVW] = 45^\circ/[001]$. Snapshots depicting the atomic structures at simulation times of (a) $t = 0$ (initial after the temperature ramp-up step), (b) $t = 34$ ns, (c) $t = 37.4$ ns, and (d) $t = 40$ ns. These snapshots show GB-pore interactions and a GB break-away event. Atoms are colored according to common neighbor analysis (CNA), where green (black) denote FCC (none) ordering.

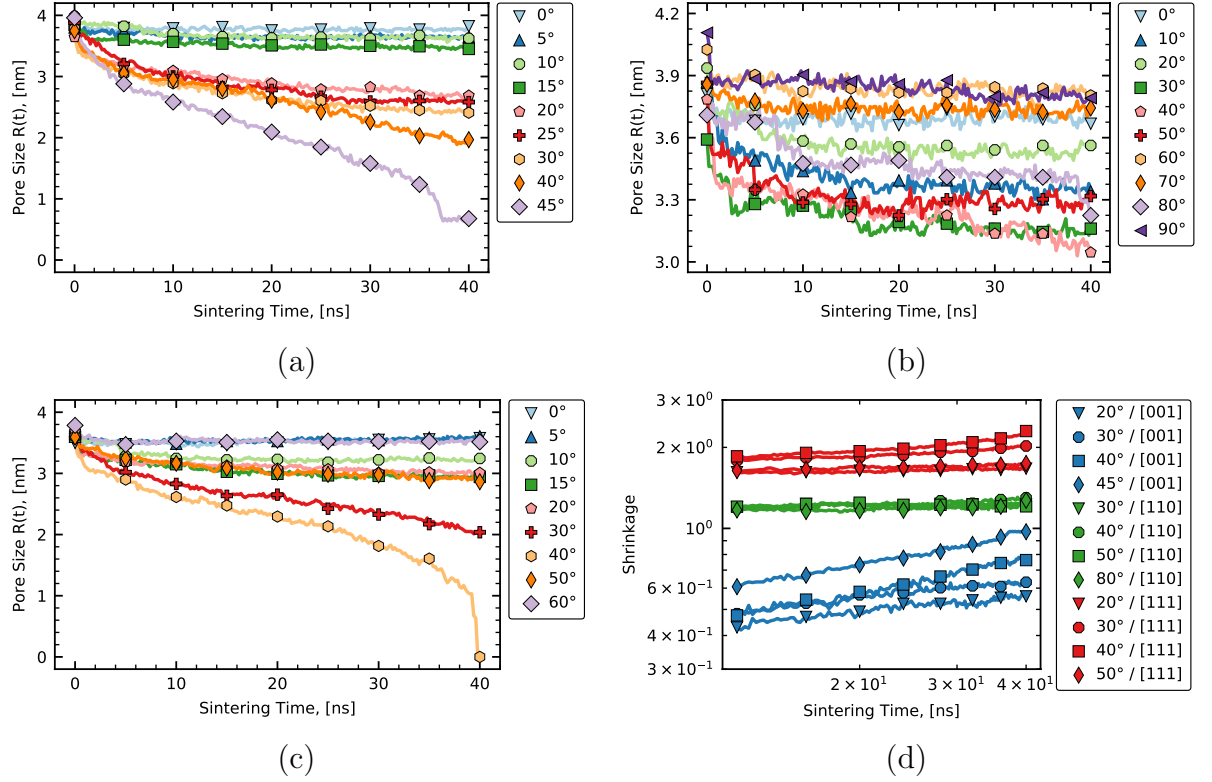


Figure 12: For the three-particle geometry: (a)–(c) Temporal evolution of the internal pore size $R(t)$ as a function of $\theta/2$ for a rotation axis $[UVW]$ of (a) $[001]$, (b) $[110]$, and (c) $[111]$. (d) On a log-log scale, a plot of pore shrinkage $S(t)$ for various combinations of $\theta/2$ and $[UVW]$.

explored in this study results in the formation of two asymmetric tilt GBs with a misorientation angle of $\theta/2$ (between particles 1-2 and 1-3) and one symmetric tilt GB with a misorientation angle of θ (between particles 2-3). Therefore, differences in pore shrinkage kinetics shown in Fig. 12 are due to different combinations of GB types, or lack of formation of all three GBs as in the case of $\theta/2 = 60^\circ$ about $[111]$, as seen in Fig. 9(i).

Next, based on Eq. 1 the temporal evolution of the pore shrinkage $S(t)$ is calculated from the data in Fig. 12(a)-(c) for all θ and $[UVW]$ cases and plotted in Fig. 12(d) on a log-log scale. It can be seen that the trends suggest power law kinetics for pore shrinkage. Systems with $[UVW] = [110]$ exhibit the slowest shrinkage rates as evident by the flat profiles in Fig. 12(d). Pore

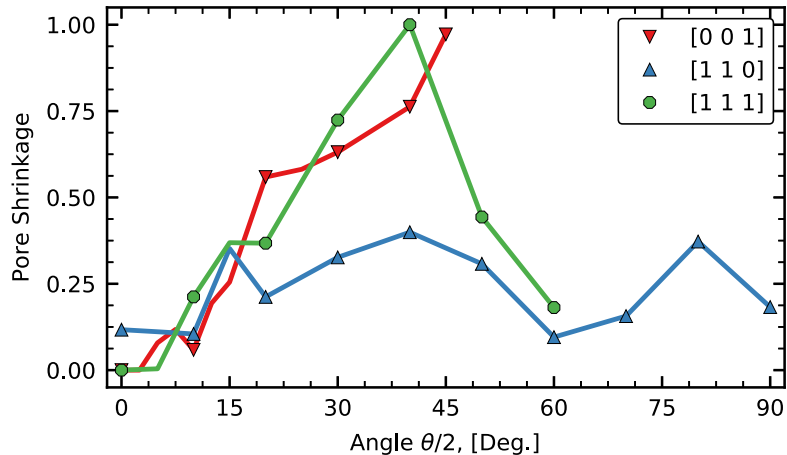


Figure 13: For the three-particle geometry, pore shrinkage at $t = 40$ ns as a function of $\theta/2$ for $[UVW] = [001], [110],$ and $[111]$.

shrinkage values at the end of sintering simulations ($t = 40$ ns) are obtained from Fig. 12(d) for each $(\theta/2)/[UVW]$ case and the results are shown in Fig. 13. It can be seen that drastic differences in pore shrinkage rates exist as a function of the GBs present in the systems. For rotations about $[001]$, pore shrinkage increases with $\theta/2$, while for $[111]$ rotations it increases with the angle until $\theta/2 = 40^\circ$. Systems with rotations about $[110]$ exhibit shrinkage rates that are lower than the ones with $[001]$ and $[111]$. Finally, it can be seen that several systems reach shrinkage values of one indicating complete shrinkage and full densification, see Fig. 9(h) for an example. The results depicted in Figs. 12 and 13 clearly highlight the paramount role that GBs play on sintering kinetics, pore shrinkage, and densification rates. For a given rotation axis $[UVW]$, a slight change in the angle $\theta/2$ can change the system's sintering behavior from rapid pore shrinkage to a stagnant one with no or very little densification.

4. Summary and Future Outlook

In this study, MD simulations were applied to examine the role of GBs on the sintering behavior of nanoscale nickel particles. Two geometries, two- and three-particle configurations, were used in this work in order to investigate

sintering kinetics, pore shrinkage, and densification rates as a function of GB character.

For the two-particle geometry, several misorientation angles and particle sizes were explored in order to systematically study their effect on particle neck formation and growth, and crystallographic re-orientation events. Simulation results suggest that particle re-orientation dominates in the small angle and particle size regimes. It was found that for angles $\theta < 25^\circ$, the two particles underwent rigid body rotation regardless of their size, which in turn led to a re-alignment of their crystallographic orientations across the particle neck region and no GB formed. The sintering behavior was quantified by monitoring the temporal evolution of the particle neck width and total free surface area, which are then used to obtain the relative GB self diffusion rates as a function of the misorientation angle.

Next, the three-particle geometry was explored, where three equi-sized cylindrical disks (particles) sharing their out-of-plane $[UVW]$ crystal axis were placed such that their centers formed the vertices of an equilateral triangle and resulted in the formation of a closed internal pore. Several orientations about the common axis were examined, and the effective internal pore size and overall pore shrinkage were monitored a function of time. Simulation results revealed a wide range of pore shrinkage profiles ranging from complete shrinkage to stagnant response with no or very little shrinkage depending on the GBs present in the systems.

Our atomistic simulation results highlight the need to account for GB anisotropic effects in mesoscopic models of sintering in order to quantitatively capture pore shrinkage and densification rates of powder compacts. Our results reveal that some GBs are effective in terms of sintering and rapid densification. This suggests the possibility of exploring “GB-engineered” concepts in sintering applications, where particles can be preferentially oriented to yield GB misorientations that optimize the sintering behavior.

Acknowledgments

This work is supported by the Laboratory Directed Research and Development program at Sandia National Laboratories, a multi-mission laboratory managed and operated by National Technology and Engineering Solutions of Sandia, LLC., a wholly owned subsidiary of Honeywell International, Inc., for the U.S. Department of Energy’s National Nuclear Security Administration

under contract DE-NA0003525. JS acknowledges support by the National Science Foundation grant IGERT-1258425.

References

- [1] M. N. Rahaman, *Ceramic Processing and Sintering*, 2nd ed., Marcel Dekker, 2003.
- [2] R. M. German, *Sintering Theory and Practice*, Wiley, 1996.
- [3] R. K. Bordia, S.-J. Kang, E. A. Olevsky, Current understanding and future research directions at the onset of the next century of sintering science and technology, *J. Amer. Ceram. Soc.* 100 (2017) 2314–2352.
- [4] R. Balluffi, S. Allen, W. Carter, *Kinetics of Materials*, Wiley, 2005.
- [5] C. Jiten, R. Gaur, R. Laishram, K. Singh, Effect of sintering temperature on the microstructural, dielectric, ferroelectric and piezoelectric properties of (na_{0.5}ko_{0.5})nbo₃ ceramics prepared from nanoscale powders, *Ceramics International* 42 (2016) 14135–14140.
- [6] S. Weyrauch, C. Wagner, C. Suckfuell, A. Lotnyk, W. Knolle, J. W. Gerlach, S. G. Mayr, Nanoporous gold synthesized by plasma-assisted inert gas condensation: room temperature sintering, nanoscale mechanical properties and stability against high energy electron irradiation, *Journal of Physics D* 51 (2018) 065301.
- [7] H. W. Zhang, R. Gopalan, T. Mukai, K. Hono, Fabrication of bulk nanocrystalline fe-c alloy by spark plasma sintering of mechanically milled powder, *Scripta Mater.* 53 (2005) 863–868.
- [8] J. A. Lewis, Direct ink writing of 3D functional materials, *Adv. Func. Mater.* 16 (2006) 2193–2204.
- [9] K. Sun, T.-S. Wei, B. Ahn, J. Seo, S. Dillon, J. Lewis, 3D printing of interdigitated Li-Ion microbattery architectures, *Adv. Mater.* 25 (2013) 4539–4543.
- [10] M. Saleh, C. Hu, R. Panat, Three-dimensional microarchitected materials and devices using nanoparticle assembly by pointwise spatial printing, *Science Adv.* 3 (2017).

- [11] M. Markl, C. Korner, Multiscale modeling of powder bed-based additive manufacturing, *Ann. Rev. Mater. Res.* 46 (2016) 93–123.
- [12] R. M. German, J. Ma, X. Wang, E. Olevsky, Processing model for tungsten powders and extension to nanoscale size range, *Powder Metallurgy* 49 (2006) 19–27.
- [13] Z. H. Zhang, F. C. Wang, S. K. Lee, Y. Liu, J. W. Cheng, Y. Liang, Microstructure characteristic, mechanical properties and sintering mechanism of nanocrystalline copper obtained by sps process, *Mater. Sci. Eng. A* 523 (2009) 134–138.
- [14] M. Ardestani, H. R. Rezaie, H. Arabi, H. Razavizadeh, The effect of sintering temperature on densification of nanoscale dispersed w-20-40%wt cu composite powders, *Int. J. Ref. Met. Hard Mater.* 27 (2009) 862–867.
- [15] P. Buffat, J.-P. Borel, Size effect on the melting temperature of gold particles, *Phys. Rev. A* 13 (1976) 2287–2298.
- [16] J. R. Greer, R. A. Street, Thermal cure effects on electrical performance of nanoparticle silver inks, *Acta Mater.* 55 (2007) 6345–6349.
- [17] G. Theunissen, A. Winnubst, A. Burggraaf, Sintering kinetics and microstructure development of nanoscale y-tzp ceramics, *J. Eur. Ceram. Soc.* 11 (1993) 315–324.
- [18] B. Srinivasarao, K. Oh-Ishi, T. Ohkubo, K. Hono, Bimodally grained high-strength fe fabricated by mechanical alloying and spark plasma sintering, *Acta Mater.* 57 (2009) 3277–3286.
- [19] M. Park, C. Schuh, Accelerated sintering in phase-separating nanostructured alloys, *Nature Comm.* 6 (2015) 6858.
- [20] S. Zhang, H. Sha, R. H. R. Castro, R. Faller, Atomistic modeling of la₃+ doping segregation effect on nanocrystalline yttria-stabilized zirconia, *Phys. Chem. Chem. Phys.* 20 (2018) 13215–13223.
- [21] A. L. Maximenko, E. A. Olevsky, Effective diffusion coefficients in solid-state sintering, *Acta Mater.* 52 (2004) 2953–2963.
- [22] F. Li, J. Pan, Modelling "Nano-Effects" in Sintering, *Engineering Materials* 35 (2013).

- [23] M. Asoro, D. Kovar, Y. Shao-Horn, L. Allard, P. Ferreira, Coalescence and sintering of pt nanoparticles: in situ observation by aberration-corrected haadf stem, *Nanotechnology* 21 (2010) 025701.
- [24] R. Chaim, G. Chevallier, A. Weibel, C. Estournès, Grain growth during spark plasma and flash sintering of ceramic nanoparticles: a review, *J. Mater. Sci.* 53 (2018) 3087–3105.
- [25] G. Kuczynski, Self-diffusion in sintering of metallic particles, *Trans. Amer. Inst. Min. Metall. Eng.* 185 (1949) 169–178.
- [26] W. Kingery, M. Berg, Study of the initial stages of sintering solids by viscous flow, evaporation-condensation, and self-diffusion, *J. App. Phys.* 26 (1955) 1205–1212.
- [27] R. Coble, Initial sintering of alumina and hematite, *J. Amer. Ceram. Soc.* 41 (1958) 55–62.
- [28] J. D., C. I., Diffusion sintering .1. initial stage sintering models and their application to shrinkage of powder compacts, *J. Amer. Ceram. Soc.* 46 (1963) 541–545.
- [29] A. Moitra, S. Kim, S. G. Kim, S. J. Park, R. M. German, M. F. Horstemeier, Investigation on sintering mechanism of nanoscale tungsten powder based on atomistic simulation, *Acta Mater.* 58 (2010) 3939–3951.
- [30] V. Randle, *The measurement of grain boundary geometry*, Taylor & Francis, 1993.
- [31] D. L. Olmsted, S. M. Foiles, E. a. Holm, Survey of computed grain boundary properties in face-centered cubic metals: I. Grain boundary energy, *Acta Mater.* 57 (2009) 3694–3703.
- [32] D. L. Olmsted, E. a. Holm, S. M. Foiles, Survey of computed grain boundary properties in face-centered cubic metals-II: Grain boundary mobility, *Acta Mater.* 57 (2009) 3704–3713.
- [33] J. Rufner, D. Anderson, K. Van Benthem, R. H. Castro, Synthesis and sintering behavior of ultrafine (<10 nm) magnesium aluminate spinel nanoparticles, *J. Amer. Ceram. Soc.* 96 (2013) 2077–2085.

- [34] A. M. Pourrahimi, D. Liu, V. Ström, M. S. Hedenqvist, R. T. Olsson, U. W. Gedde, Heat treatment of zno nanoparticles: new methods to achieve high-purity nanoparticles for high-voltage applications, *J. Mater. Chem. A* 3 (2015) 17190–17200.
- [35] J. E. Bonevich, L. D. Marks, The sintering behavior of ultrafine alumina particles, *J. Mater. Res.* 7 (1992) 1489–1500.
- [36] J.-S. Lee, J.-P. Choi, G.-Y. Lee, Consolidation of hierarchy-structured nanopowder agglomerates and its application to net-shaping nanopowder materials, *Materials* 6 (2013) 4046–4063.
- [37] R. Theissmann, M. Fendrich, R. Zinetullin, G. Guenther, G. Schierning, D. E. Wolf, Crystallographic reorientation and nanoparticle coalescence, *Phys. Rev. B* 78 (2008) 1–10.
- [38] J. Raut, R. Bhagat, K. Fichtorn, Sintering of aluminum nanoparticles: A molecular dynamics study, *Nanostruct. Mater.* 10 (1998) 837 – 851.
- [39] B. J. Henz, T. Hawa, M. Zachariah, Molecular dynamics simulation of the energetic reaction between ni and al nanoparticles, *J. Appl. Phys.* 105 (2009) 124310.
- [40] J.-H. Shim, B.-J. Lee, Y. W. Cho, Thermal stability of unsupported gold nanoparticle: a molecular dynamics study, *Surf. Sci.* 512 (2002) 262 – 268.
- [41] M. R. Zachariah, M. J. Carrier, Molecular dynamics computation of gas-phase nanoparticle sintering: a comparison with phenomenological models, *J. Aerosol Sci.* 30 (1999) 1139 – 1151.
- [42] T. Hawa, M. Zachariah, Coalescence kinetics of unequal sized nanoparticles, *J. Aerosol Sci.* 37 (2006) 1 – 15.
- [43] Y. Zhang, J. Zhang, Sintering phenomena and mechanical strength of nickel based materials in direct metal laser sintering process—a molecular dynamics study, *J. Mater. Res.* 31 (2016) 2233–2243.
- [44] B. J. Henz, T. Hawa, M. Zachariah, Molecular dynamics simulation of the kinetic sintering of ni and al nanoparticles, *Molecular Simulation* 35 (2009) 804–811.

- [45] H. A. Alarifi, M. Atis, C. Ozdogan, A. Hu, M. Yavuz, Y. Zhou, Molecular Dynamics Simulation of Sintering and Surface Premelting of Silver Nanoparticles, *Mater. Trans.* 54 (2013) 884–889.
- [46] P. Zeng, S. Zajac, P. Clapp, J. Rifkin, Nanoparticle sintering simulations, *Mater. Sci. Eng. A* 252 (1998) 301 – 306.
- [47] Y. Zhang, L. Wu, H. El-Mounayri, K. Brand, J. Zhang, Molecular dynamics study of the strength of laser sintered iron nanoparticles, *Procedia Manufacturing* 1 (2015) 296 – 307.
- [48] R. Balluffi, T. Kwok, P. Bristowe, A. Brokman, P. Ho, S. Yip, Determination of vacancy mechanism for grain boundary self-diffusion by computer simulation, *Scripta Metall.* 15 (1981) 951 – 956.
- [49] L. Ding, R. L. Davidchack, J. Pan, A molecular dynamics study of sintering between nanoparticles, *Comp. Mater. Sci.* 45 (2009) 247–256.
- [50] P. Song, D. Wen, Molecular dynamics simulation of the sintering of metallic nanoparticles, *J. Nanopar. Res.* 12 (2010) 823–829.
- [51] S. Arcidiacono, N. R. Bieri, D. Poulikakos, C. P. Grigoropoulos, On the coalescence of gold nanoparticles, *Int. J. Multiphase Flow* 30 (2004) 979–994.
- [52] A. P. Lange, A. Samanta, H. Majidi, S. Mahajan, J. Ging, T. Y. Olson, K. van Benthem, S. Elhadj, Dislocation mediated alignment during metal nanoparticle coalescence, *Acta Mater.* 120 (2016) 364–378.
- [53] D. Rowenhorst, A. D. Rollett, G. S. Rohrer, M. Groeber, M. Jackson, P. J. Konijnenberg, M. D. Graef, Consistent representations of and conversions between 3d rotations, *Mod. Sim. Mater. Sci. Eng.* 23 (2015).
- [54] S. M. Foiles, J. J. Hoyt, Computation of grain boundary stiffness and mobility from boundary fluctuations, *Acta Mater.* 54 (2006) 3351–3357.
- [55] S. Plimpton, Fast Parallel Algorithms for Short – Range Molecular Dynamics, *J. Comp. Phys.* 117 (1995) 1–19.
- [56] S. Plimpton, LAMMPS, <http://lammps.sandia.gov>, 2018.

- [57] A. Stukowski, Visualization and analysis of atomistic simulation data with OVITO—the Open Visualization Tool, *Mod. Sim. Mater. Sci. Eng.* 18 (2010) 015012.
- [58] S. Nose, A unified formulation of the constant temperature molecular dynamics methods, *J. Chem. Phys.* 81 (1984) 511–519.
- [59] W. G. Hoover, Canonical dynamics: Equilibrium phase-space distributions, *Phys. Rev. A* 31 (1985) 1695–1697.
- [60] W. Shinoda, M. Shiga, M. Mikami, Rapid estimation of elastic constants by molecular dynamics simulation under constant stress, *Phys. Rev. B* 69 (2004) 134103.
- [61] A. Stukowski, Computational analysis methods in atomistic modeling of crystals, *JOM* 66 (2014) 399–407.
- [62] D. L. Johnson, New method of obtaining volume, grain-boundary, and surface diffusion coefficients from sintering data, *J. Appl. Phys.* 40 (1969) 192–200.
- [63] D. L. Johnson, New method of obtaining volume, grain-boundary, and surface diffusion coefficients from sintering data, *J. Appl. Phys.* (1969).
- [64] W. D. Kingery, M. Berg, Study of the initial stages of sintering solids by viscous flow, evaporation-condensation, and self-diffusion, *J. Appl. Phys.* 26 (1955) 1205–1212.
- [65] H. Collins, P. G. Shewmon, Effect of adsorbed sulfur on surface self-diffusion of copper, *Trans. AIME* 236 (1966) 1354.
- [66] P. G. SHEWMON, J. CHOI, Anisotropy of surface diffusion coefficient for copper, *Trans. AIME* 227 (1963) 515.
- [67] H. K. D. H. Bhadeshia, *Geometry of Crystals, Polycrystals, and Phase Transformations*, CRC Press, 2018.
- [68] J. C. Fisher, Calculation of diffusion penetration curves for surface and grain boundary diffusion, *J. App. Phys.* 22 (1951) 74–77.
- [69] J. Bocquet, G. Brebec, Y. Limoge, Diffusion in metals and alloys, in: R. W. Cahn, P. Haasen (Eds.), *Physical Metallurgy*, Elsevier, Amsterdam, 1996, pp. 619–632.